*Article*

# Wireless Diagnosis and Control of DC–DC Converter for Off-Grid Photovoltaic Systems

Reda El Abbadi [1,†] , Mohamed Aatabe [2,†] and Allal El Moubarek Bouzid [3,*]

1 LAMISNE, Polydisciplinary Faculty of Taroudant, Ibn Zohr University, Agadir P.O. Box 8106, Morocco; reda.elabbadi@edu.uiz.ac.ma
2 LISTI, National School of Applied Sciences, Ibn Zohr University, Agadir P.O. Box 1136, Morocco; aatabe.mohamed@gmail.com
3 Research and Higher Education Department, ICAM School of Engineering, Toulouse Campus, 75 av. de Grande Bretagne, 31076 Toulouse, France
* Correspondence: allal.el.moubarek.bouzid@uqtr.ca
† These authors contributed equally to this work.

**Abstract:** Integrating a photovoltaic (PV) microgrid system with wireless network control heralds a new era for renewable energy systems. This fusion capitalizes on the strengths of photovoltaic technology, leveraging solar energy for electricity generation while incorporating advanced networked control capabilities. Although employing network communication to facilitate information exchange among system elements offers benefits, it also introduces novel challenges which can hinder fault diagnosis, such as packet loss and communication delay. This paper focuses on a cloud-based fault detection approach for an effective boost converter within a photovoltaic system. Faults are diagnosed using a detection algorithm based on the Lyapunov function, ensuring power optimization. The effectiveness of our approach is demonstrated through simulations of a PV generator model utilizing real-time weather data collected in Brazil, illustrating its robustness through the acquired results.

**Keywords:** photovoltaic microgrid system; maximum power point tracking; networked control system; packet dropout; fault detection

## 1. Introduction

A photovoltaic system harnesses sunlight to generate electricity through the photovoltaic effect, with semiconductor cells producing voltage and current when exposed to light [1,2]. These cells are commonly made of monocrystalline or polycrystalline silicon [3]. Groupings of photovoltaic cells can be interconnected either in series to achieve the desired voltage, or in parallel to achieve the desired current [4].

An off-grid photovoltaic system typically depends on a battery bank, which serves a pivotal function in storing the electricity generated during sunny periods, thereby guaranteeing a continuous supply even at night. Alongside batteries, these systems commonly integrate charge controllers to manage energy flow and inverters to convert DC electricity into AC. Collectively, these components operate in synergy to furnish a robust and self-sustaining source of electricity.

Current systems are increasingly interconnected and possess large dimensions, making point-to-point connection unachievable and infeasible. For this reason, network become a smart choice, as data can be transformed between the system components through a communication network [5–7]. Nevertheless, despite the advantages of adopting networks to transmit data, new problems such as packet loss and delay appear [8]. Recently, there has been growing buzz surrounding networked photovoltaic systems. These systems have gained significant attention in recent times, indicating their increasing importance and relevance in the field of renewable energy [9–11]. Networked photovoltaic systems contain

many interconnected devices and that exchange data over the network, with examples including temperature and solar radiation sensors, mediated by a controller.

Due to thermal stress, failures can occur in the photovoltaic system. Short and open circuit faults are considered the most common failures in power semiconductor devices [12]. Power semiconductor devices stand out as the most vulnerable components in power electronics. Many failures are linked to the boost DC–DC converter within photovoltaic system. Consequently, implementing a fault detection and isolation (FDI) scheme becomes imperative as a means to enhance accuracy and reliability [13].

The impact of faults in a networked control system (NCS) mirrors that in a point-to-point system in that a fault in any component can potentially destabilize the entire global system; consequently, ensuring system security becomes a paramount concern. The Fault Detection and Isolation (FDI) approach has demonstrated its efficacy as a powerful technique for enhancing system safety [14]. This technique not only detects the occurrence of a fault, it can identify its location and estimate its amplitude. However, occasional packet loss during transmission can adversely affect the diagnostic process.

Several studies have explored the controller and diagnostic aspects of networked photovoltaic systems. The authors of [10] introduced an economical real-time cyber–physical system tailored for remote monitoring of solar energy installations. This system employed an Arduino Nano equipped with sensors for measuring current, voltage, light intensity, dust, humidity, and temperature. These sensors were utilized to assess system performance and analyze the influence of different parameters on power generation. Using a GSM module, the gathered data were transmitted to a freely available and open-source cloud platform for processing, storage, analysis, and the execution of preemptive measures aimed at enhancing power generation capacity. The study presented in [9] explored the creation of an intelligent photovoltaic module integrated with a wireless sensor network and software for real-time monitoring and control of a photovoltaic system at the module level. Sensor data were gathered periodically and sent to a central base station. Power control was executed through an integrated DC–DC converter, with the converter's output voltage regulated by a digital controller. Remote monitoring and distributed control data were transmitted efficiently through a cost-effective ZigBee wireless network. The authors of [15] implemented wireless control for a grid-connected PV system to ensure proper operation. This was achieved by wirelessly controlling both the DC–DC converter and the DC–AC converter in the grid-connected PV system. A novel approach for monitoring a grid-connected PV system was introduced in [16], where each PV module was monitored through a Wireless Sensor Network (WSN) to identify any defective individual modules. The authors of [17] proposed a Zigbee-based monitoring system tailored for a grid-connected PV system. The monitored parameters included PV voltage, PV current, inverter voltage, inverter current, ambient temperature, module temperature, and solar irradiation. The system adopted a point-to-point network topology employing a straightforward Zigbee configuration with a transmission range of up to 100 m in line-of-sight conditions.

The aforementioned research efforts in the field have centered on optimizing the performance of PV systems and addressing their challenges, with a predominant focus on their electronic components and operational aspects. Seeking to enhance the efficiency and reliability of PV systems, these studies have delved into areas such as power conversion, control algorithms, and hardware design. However, only a relatively limited number of studies have explored the communication aspect of PV systems. This encompasses investigating issues related to data transmission, network reliability, and real-time monitoring, all of which are crucial for ensuring seamless operation and optimizing performance. Among the challenges within this domain are packet dropout, where data packets fail to reach their destination, and communication delay, which can affect the timeliness and accuracy of system monitoring and control. Hence, this paper contributes to addressing these communication challenges for robust and dependable PV system operation, especially in applications requiring high levels of reliability and performance.

The main contribution of this paper lies in its exploration of wireless control and diagnostic methodologies for PV systems. Acknowledging the likelihood of packet dropout in communication links, this study devises a networked filter solution by resolving a linear matrix inequality. This filter is engineered to swiftly identify faults as they occur, facilitating rapid and effective intervention by the controller. The efficacy of this approach is vividly demonstrated through simulations using real-time data sourced from Goiás, Brazil. Essentially, this paper presents an innovative theoretical framework for managing photovoltaic generators, paving the way for practical applications in the field.

## 2. Photovoltaic Panel Model

A photovoltaic panel is a set of many photovoltaic cells connected in series and in parallel to form one PV unit with the required current and voltage levels. Typically, the PV panel is integrated with other electrical components to form a PV generator system. As illustrated in Figure 1, such a PV generator system consists of a DC–DC converter circuit connected to the PV module accompanied by a capacitor, an inductor, resistances, a diode, and a MOSFET.

To elucidate the dynamics of the PV generator, we analyze the MOSFET while operating in either "on" or "off" mode, as proposed in [18]. The system state of the PV generator is denoted as $x(t) = [v_{pv}(t), i(t), v(t)]' \in \mathbb{R}^3$, while the control input $u(t) \in [0,1]$ regulates the MOSFET duty cycle modulation.
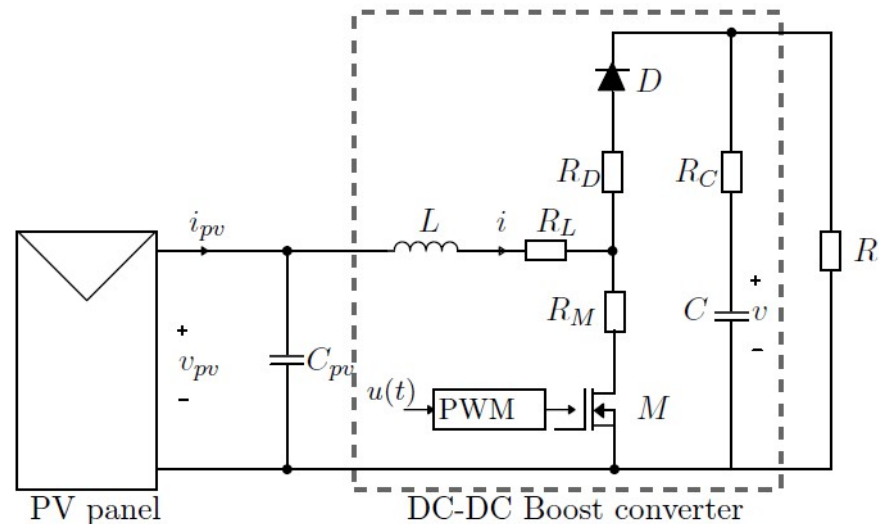


**Figure 1.** Scheme of the PV generator system.

The PV generator dynamics can be expressed as follows [19,20]:

$$\dot{x}(t) = A(x(t))x(t) + B(x(t))u(t), \quad t \geq 0, \quad x(0) = x_0 \in \mathbb{R}^3, \quad (1)$$

where the system matrices are

$$A = \begin{bmatrix} \frac{1}{C_{pv}}\frac{i_{pv}}{v_{pv}} & -\frac{1}{C_{pv}} & 0 \\ \frac{1}{L} & -\frac{R_L+R_D+\frac{R_C R}{R_C+R}}{L} & -\frac{R}{L(R_C+R)} \\ 0 & \frac{R}{C(R_C+R)} & -\frac{1}{C(R_C+R)} \end{bmatrix}, B = \begin{bmatrix} 0 \\ \frac{-R_M+R_D+\frac{R_C R}{R_C+R}}{L}i(t) + \frac{R}{L(R_C+R)}v(t) \\ -\frac{R}{C(R_C+R)}i(t) \end{bmatrix}.$$

The PV power is expressed by

$$P_{pv} = v_{pv}i_{pv},$$
$$= n_p I_{ph}v_{pv} - n_p I_{rs}v_{pv}\left(\exp\left(\frac{k_{pv}v_{pv}}{n_s}\right) - 1\right). \quad (2)$$

Considering that $k_{pv} = \frac{q}{\eta kT}$ represents the inverse of the thermal voltage, the system output is defined as the derivative of $P_{pv}$ with respect to $v_{pv}$, expressed as follows:

$$
\begin{aligned}
y(t) = \frac{dP_{pv}}{dv_{pv}} &= i_{pv} - \frac{n_p k_{pv}}{n_s} I_{rs} v_{pv} \exp\left(\frac{k_{pv} v_{pv}}{n_s}\right), \\
&= \left[\frac{i_{pv}}{v_{pv}} - \frac{n_p k_{pv}}{n_s} I_{rs} \exp(\frac{k_{pv} v_{pv}}{n_s}) \quad 0 \quad 0\right] x(t). \\
&= C x(t).
\end{aligned}
\tag{3}
$$

The intricate nature of the nonlinear System (1) presents challenges to analysis. Endeavoring to surmount these complexities, we opt to reformulate System (1) using the Takagi–Sugeno (T-S) fuzzy approach. Transitioning from continuous time to discrete time, the differential Equation (1) can be discretized using the first-order Euler technique. In this approach, $\dot{x}(t)$ is replaced by $\frac{x(k+1)-x(k)}{T_e}$, where $T_e$ denotes the sampling time. Consequently, the differential Equation (1) transforms into

$$
\begin{aligned}
x(k+1) &= \bar{A} x(k) + \bar{B} u(k), \\
y(k+1) &= \bar{C} x(k),
\end{aligned}
\tag{4}
$$

where the system matrices are

$$
\bar{A} = \begin{bmatrix} 1 + \frac{T_e}{C_{pv}} \frac{i_{pv}}{v_{pv}} & -\frac{T_e}{C_{pv}} & 0 \\ \frac{T_e}{L} & 1 - T_e \frac{R_L + R_D + \frac{R_C R}{R_C + R}}{L} & -T_e \frac{R}{L(R_C + R)} \\ 0 & -T_e \frac{R}{C(R_C + R)} & 1 - \frac{T_e}{C(R_C + R)} \end{bmatrix},
$$

$$
\bar{B} = \begin{bmatrix} 0 \\ T_e \frac{-R_M + R_D + \frac{R_C R}{R_C + R}}{L} i(t) + T_e \frac{R}{L(R_C + R)} v(t) \\ -T_e \frac{R}{C(R_C + R)} i(t) \end{bmatrix},
$$

$$
\bar{C} = \left[\frac{i_{pv}}{v_{pv}} - \frac{n_p k_{pv}}{n_s} I_{rs} \exp(\frac{k_{pv} v_{pv}}{n_s}) \quad 0 \quad 0\right].
$$

The handling of the nonlinear System (4) poses significant challenges. To address this difficulty, we have adopted the TS fuzzy approach to reframing the system (4).

*TS Fuzzy Modelling*

The TS fuzzy methodology proves valuable in characterizing nonlinear systems by employing a blend of localized linear subsystems governed by "IF–THEN" rules. Each of these subsystems is influenced by a membership function, as indicated by Tanaka et al. [21]. Our subsequent step involves transforming the representation of the nonlinear PV system (1) into a T-S fuzzy representation. In accomplishing this, we delineate the constituent elements of the premise-variable vector $z(t) = [z_1(k), z_2(k), z_3(k), z_4(k)]'$ as follows:

$$
z_1(k) = \frac{i_{pv}(k)}{v_{pv}(k)}, \; z_2(k) = i(k), \; z_3(k) = v(k), \; z_4(k) = \frac{n_p k_{pv}}{n_s} I_{rs} \exp(\frac{k_{pv} v_{pv}(k)}{n_s}).
$$

Consider the following fuzzy rules:

**Rule p**: **IF** $z_1(k)$ **is** $M_{p,1}$ **and** $\ldots z_\mu(k)$ **is** $M_{p,\mu}$ **THEN**

$$\bar{A}_p = \begin{bmatrix} 1 + \frac{T_e}{C_{pv}}z_{p,1} & -\frac{T_e}{C_{pv}} & 0 \\ \frac{T_e}{L} & 1 - T_e\frac{R_L+R_D+\frac{R_C R}{R_C+R}}{L} & -T_e\frac{R}{L(R_C+R)} \\ 0 & T_e\frac{R}{C(R_C+R)} & 1 - \frac{T_e}{C(R_C+R)} \end{bmatrix},$$

$$\bar{B}_p = \begin{bmatrix} 0 \\ T_e\frac{-R_M+R_D+\frac{R_C R}{R_C+R}}{L}z_{p,2} + T_e\frac{R}{L(R_C+R)}z_{p,3} \\ -T_e\frac{R}{C(R_C+R)}z_{p,2} \end{bmatrix},$$

$$\bar{C}_p = \begin{bmatrix} z_{p,1} - z_{p,4} & 0 & 0 \end{bmatrix}.$$

The membership function associated with the $p$-th subsystem is defined as follows:

$$h_p(z(k)) = \frac{M_p(z(k))}{\sum\limits_{p=1}^{s} M_p(z(k))}, \quad M_p(z(k)) = \prod_{j=1}^{\mu} M_{p,j}(z_j(k))$$

with the following constraints:

$$\sum_{p=1}^{s} h_p(z(k)) = 1, \qquad 0 \le h_p(z(k)) \le 1, \ \ p \in \mathcal{M} := \{1,\ldots,s\}, \tag{5}$$

where $s$ denotes the number of fuzzy rules and $M_{p,j}(z_j(k))$ refers to the membership activation degree of $z_j(k) \in [z_j^\ell \ \ z_j^u]$ in fuzzy set $M_{p,j}$, described by the general form

$$M_j^\ell = \frac{z_j^u - z_j(k)}{z_j^u - z_j^\ell}, \quad M_j^u = \frac{z_j(k) - z_j^\ell}{z_j^u - z_j^\ell}. \tag{6}$$

Finally, the T-S fuzzy model of the PV generator reads as follows:

$$
\begin{aligned}
x(k+1) &= \sum_{p=1}^{s} h_p(z(k))(\bar{A}_p x(k) + \bar{B}_p u(k)), \ x(0) = x_0 \in \mathbb{R}^n, \\
y(k) &= \sum_{p=1}^{s} h_p(z(k))\bar{C}_p x(k),
\end{aligned}
\tag{7}
$$

where the matrices $\bar{A}_p$, $\bar{B}_p$, and $\bar{C}_p$ for $p \in \{1,\ldots,s\}$ are derived based on various permutations of the premise-variables.

## 3. Networked Control System Model

The literature presents two models of the NCS, which are distinguished by the location of the wireless network within the global structure. The network can exist either between the sensor and controller (S–C) or between the controller and actuator (C–A), as illustrated in Figure 2. One well-known challenge associated with wireless networks is packet dropout, which has been extensively investigated in various studies. Numerous mathematical models addressing this constraint have been put forward. The packet dropout process is often conceptualized as a binary switching sequence described by a Bernoulli process utilizing probability theory [22].
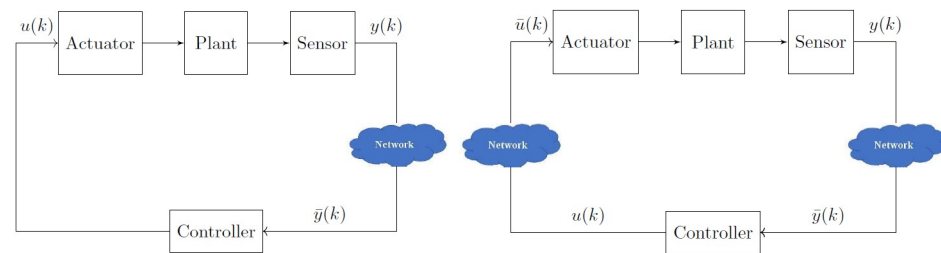
**Figure 2.** Structure of an NCS.

In this study, we assume the presence of packet loss simultaneously in both S–C and C–A models, as depicted in Figure 3. The wireless network is conceptualized as a switch, denoted as $S_i$, with $i = 1, 2$, that intermittently opens and closes. The opening of the switch signifies the occurrence of packet loss, while its closure indicates successful packet transmission. The dynamics of switches $S_1$ and $S_2$ can be expressed as follows:

$$\begin{cases} \bar{y}(k) = \alpha(k)\, y(k) + (1 - \alpha(k))\, y(k - 1), \\ \bar{u}(k) = \beta(k)\, u(k) + (1 - \beta(k)) u(k - 1), \end{cases} \tag{8}$$

where

$$\alpha(k), \beta(k) = \begin{cases} 0 \text{ if the packet is lost,} \\ 1 \text{ otherwise.} \end{cases} \tag{9}$$
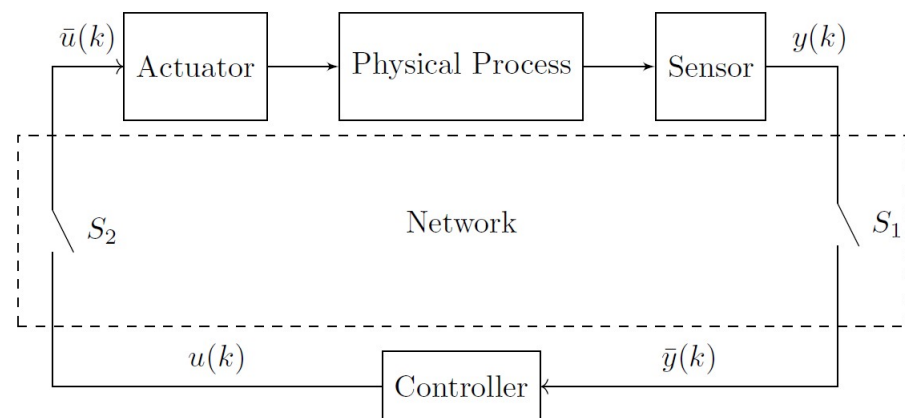


**Figure 3.** Packet dropout model.

From (8) and (9), random data packet dropout can be modeled as a discrete-time homogeneous Markov chain $\mu(k)$ with the four modes shown in Table 1.

**Table 1.** Values of $\mu(k)$.

| $\mu(k)$ | $\alpha$ | $\beta$ | Switch $S_1$ | Switch $S_2$ |
|----------|----------|---------|--------------|--------------|
| 1 | 0 | 0 | off | off |
| 2 | 0 | 1 | off | on |
| 3 | 1 | 0 | on | off |
| 4 | 1 | 1 | on | on |

The transition probability of the variable $\mu(k)$ can be expressed as

$$Prob\{\mu(k+1) = j | \mu(k) = i\} = \Pi_{ij}, \tag{10}$$

where the elements of the matrix $\Pi$ should respect two mathematical conditions: $\Pi_{ij} \geq 0$ for all $i, j \in [1, 4]$, and $\sum_{j=1}^{4} \Pi_{ij} = 1$.

## 4. Wireless Control-Based Power Optimization for PV System

This section presents an innovative power optimization strategy for networked PV systems. The strategy is outlined in the following sequence to provide a comprehensive understanding of its synthesis.

### 4.1. Networked PV System

Network communication is an indispensable element of networked PV systems (see Figure 4). This digital infrastructure enhances the efficiency, reliability, and sustainability of PV generators, making networked PV systems a promising solution for a cleaner and smarter energy future.
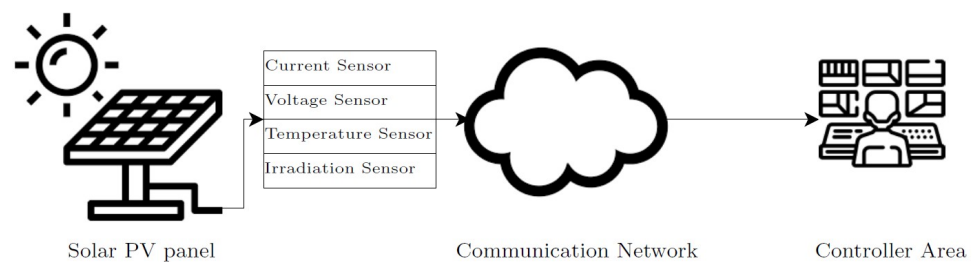


**Figure 4.** Scheme of a networked PV system.

In a networked photovoltaic system, the role of the communication network is essential for enabling effective control and monitoring of the entire solar energy setup. Network connectivity facilitates real-time data exchange between all system components. One of the principal roles of network communication in a networked PV system is remote monitoring. Through network connections, system operators and homeowners can access a wealth of data regarding the performance of solar panels, inverters, and energy storage devices. This remote monitoring capability allows them to track energy generation, consumption, and storage levels, providing valuable insights into system health and efficiency.

Moreover, network communication enables remote control and adjustment of system settings. For instance, operators can remotely configure the duty cycle of the DC–DC converter or adjust the charging and discharging profiles of energy storage systems, ensuring optimal performance and the ability to adapt to changing energy demands.

In addition to the above-mentioned advantages, communication networks plays a crucial role in predictive maintenance. By continuously transmitting data to centralized servers or cloud-based platforms, the system can undergo real-time analysis. This data-driven approach can identify potential issues or anomalies in the system's operation, allowing for proactive maintenance or servicing before problems escalate.

### 4.2. Cloud MPPT Control Design

The maximum power point voltage (MPPV) is the point at which a solar panel produces the most power. The MPPV varies depending on the radiance intensity and the temperature during the day. To track this point, an MPPT algorithm needs to be used. The MPPT algorithm inputs are the actual measured values of the PV output voltage and current. The MPPT algorithm output is a reference input voltage used by the PV bus voltage controller to adjust the duty cycle of the DC–DC converter, and consequently the PV output voltage [23].

In this section, a cloud closed-loop MPPT control algorithm is presented. Many MPPT control algorithms can be found In the literature; however, only a few papers have taken the cloud environment into consideration. In this study, as illustrated in Figure 5, we consider that the system state and the input signals pass through a communication network.
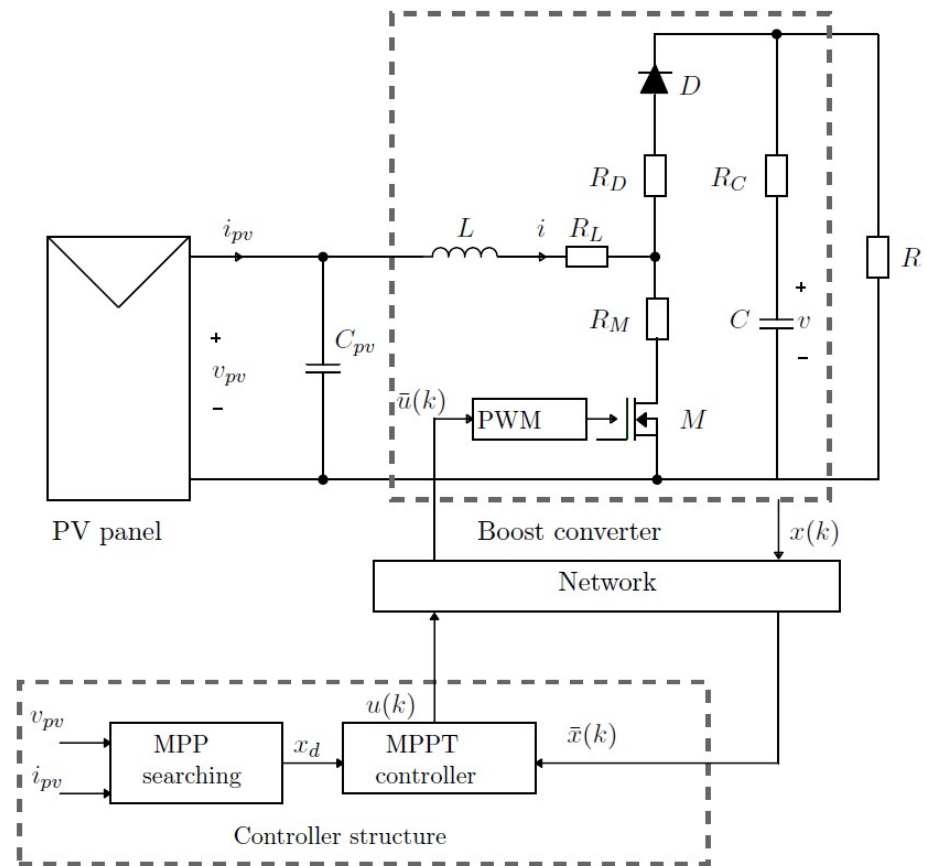
**Figure 5.** Structure of the wireless-controlled PV system.

The error signal is defined as follows:

$$
\begin{aligned}
e(k) &= y(k) - y_d(k), \\
&= \sum_{p=1}^{s} h_p(z(k)) \bar{C}_p [x(k) - x_d(k)],
\end{aligned}
\tag{11}
$$

where $x_d(k)$ represents the desired optimal trajectory of $x(k)$ aligned with the maximum power output of the PV system, corresponding to $y_d(k) = 0$. Our goal is to minimize the long-term error $e(k)$, ultimately aiming for $\lim_{k \to \infty} [y(k) - y_d(k)] = 0$.

For this purpose, we merge the error dynamics into the controlled dynamics, which (with $\bar{x}(k) = [x(k)\, e(k)]' \in \mathbb{R}^{n+1}$, and $x_b(k) = [0\, x_d(k)]' \in \mathbb{R}^{n+1}$) results in

$$
\begin{aligned}
\bar{x}(k+1) &= \sum_{p=1}^{s} h_p(z(t)) [\hat{A}_p \bar{x}(k) + \hat{B}_p \bar{u}(k) + \hat{B}_{op} x_b(k)], \\
y(k) &= \sum_{d=1}^{s} h_p(z(t)) \hat{C}_p \bar{x}(k),
\end{aligned}
\tag{12}
$$

where

$$
\hat{A}_p = \begin{bmatrix} \bar{A}_p & 0 \\ \bar{C}_p & 0 \end{bmatrix}, \ \hat{B}_p = \begin{bmatrix} \bar{B}_p \\ 0 \end{bmatrix}, \ \hat{B}_{op} = \begin{bmatrix} 0 \\ -\bar{C}_p \end{bmatrix}, \ \text{and} \ \hat{C}_p = \begin{bmatrix} \bar{C}_p & 0 \end{bmatrix}.
$$

Replacing (8) in (12), we obtain

$$
\bar{x}(k+1) = \sum_{p=1}^{s} h_p(z(t)) [\mathscr{A}_p \bar{x}(k) + \mathscr{B}_p \bar{x}(k-1) + \hat{B}_{op} x_b(k)],
\tag{13}
$$

where $\mathscr{A}_p = \hat{A}_p + \beta(k)\hat{B}_p K_p$ and $\mathscr{B}_p = (1 - \beta(k))\hat{B}_p K_p$.

Our aim is to ensure system stability while guaranteeing that the photovoltaic generator operates at its maximum power. We use $H_\infty$ to reach this objective, as follows:

$$\mathbb{E}\left[\sum_0^N [e'(k)e(k) - \gamma^2 x_d'(k)x_d(k)]\right] < 0, \gamma > 0, \tag{14}$$

with $N$ being the total number of samples.

**Theorem 1.** *For a positive constant $\gamma$, if there exist matrices $P_i > 0$ and $Q > 0$ satisfying the inequality*

$$\begin{bmatrix} -\mathscr{X}_i & \mathscr{A}_p & \mathscr{B}_p & \hat{\mathscr{B}}_{op} \\ * & -P_i + Q + (0_{1\times3}, 1) & 0 & 0 \\ * & * & -Q & 0 \\ * & * & * & -\gamma^2 \end{bmatrix} < 0, \quad i \in [1,4], \tag{15}$$

*then System (13) is asymptotically stable.*

**Proof.** To ensure the stochastic stability of System (13), we use the stochastic Lyapunov–Krasovskii functional:

$$V(\bar{x}_k, \mu_k) = V_1 + V_2, \text{ with } V_1 = \bar{x}_k' P(\mu_k)\bar{x}_k, \ V_2 = \bar{x}_{k-1}' Q\bar{x}_{k-1}. \tag{16}$$

The expectation of $\Delta V_1$ along the closed-loop system is

$$\mathbb{E}[\Delta V_1] = \bar{x}_k' \mathscr{A}_p' \bar{P}_i \mathscr{A}_p \bar{x}_k + \bar{x}_k' \mathscr{A}_p' \bar{P}_i \mathscr{B}_p \bar{x}_{k-1} + \bar{x}_k' \mathscr{A}_p' \bar{P}_i \hat{\mathscr{B}}_{op} \bar{x}_{bk} + \bar{x}_{k-1}' \mathscr{B}_p' \bar{P}_i \mathscr{B}_p \bar{x}_{k-1}$$

$$+ \bar{x}_{k-1}' \mathscr{B}_p' \bar{P}_i \hat{\mathscr{B}}_{op} \bar{x}_{bk} + \bar{x}_{bk}' \hat{\mathscr{B}}_{op}' \bar{P}_i \hat{\mathscr{B}}_{op} \bar{x}_{bk} - \bar{x}_k' P_i \bar{x}_k, \text{ with } \bar{P}_i = \sum_{j=1}^4 \pi_{ij} P_j. \tag{17}$$

The expectation of $\Delta V_2$ along the closed-loop system is

$$\mathbb{E}[\Delta V_2] = \bar{x}_k' Q\bar{x}_k - \bar{x}_{k-1}' Q\bar{x}_{k-1}. \tag{18}$$

From (16), (17), and (18) we have

$$\eta_k' \begin{bmatrix} \mathscr{A}_p' \bar{P}_i \mathscr{A}_p - P_i + Q & \mathscr{A}_p' \bar{P}_i \mathscr{B}_p & \mathscr{A}_p' \bar{P}_i \hat{\mathscr{B}}_{op} \\ * & -Q + \mathscr{B}_p' \bar{P}_i \mathscr{B}_p & \mathscr{B}_p' \bar{P}_i \hat{\mathscr{B}}_{op} \\ * & * & \hat{\mathscr{B}}_{op}' \bar{P}_i \hat{\mathscr{B}}_{op} \end{bmatrix} \eta_k < 0, \tag{19}$$

where $\eta_k = [\bar{x}_k' \ \ x_{bk}']'$.

The stability condition is then modified to incorporate the $H_\infty$ norm condition. In formal terms, the inequality in (19) is expressed as

$$\begin{bmatrix} \mathscr{A}_p' \bar{P}_i \mathscr{A}_p - P_i + Q + (0_{1\times3}, 1) & \mathscr{A}_p' \bar{P}_i \mathscr{B}_p & \mathscr{A}_p' \bar{P}_i \hat{\mathscr{B}}_{op} \\ * & -Q + \mathscr{B}_p' \bar{P}_i \mathscr{B}_p & \mathscr{B}_p' \bar{P}_i \hat{\mathscr{B}}_{op} \\ * & * & \hat{\mathscr{B}}_{op}' \bar{P}_i \hat{\mathscr{B}}_{op} - \gamma^2 \end{bmatrix} < 0. \tag{20}$$

The inequality in (20) cannot be considered as an LMI due to the presence of a nonlinear term within the matrix. Therefore, we need to manipulate the inequality to make it linear and obtain an LMI. To solve this nonlinearity problem, a Schur complement is applied, as follows:

$$\begin{bmatrix} -\bar{P}_i^{-1} & \mathscr{A}_p & \mathscr{B}_p & \hat{\mathscr{B}}_{op} \\ * & -P_i + Q + (0_{1\times3}, 1) & 0 & 0 \\ * & * & -Q & 0 \\ * & * & * & -\gamma^2 \end{bmatrix} < 0. \tag{21}$$

To eliminate the matrix $\bar{P}_i^{-1}$ in the inequality in (21), a change of variable is used in which we replace the matrix $\bar{P}_i^{-1}$ with the matrix $\mathscr{X}_i$, meaning that the inequality in (21) becomes

$$\begin{bmatrix} -\mathscr{X}_i & \mathscr{A}_p & \mathscr{B}_p & \hat{\mathscr{B}}_{op} \\ * & -P_i + Q + (0_{1\times3}, 1) & 0 & 0 \\ * & * & -Q & 0 \\ * & * & * & -\gamma^2 \end{bmatrix} < 0 \qquad (22)$$

with $\mathscr{X}_i = \bar{P}_i^{-1}$. □

## 5. Wireless Strategy-Based Diagnosis of PV Conversion Systems

In this section, we present a novel wireless strategy for fault diagnosis in the DC–DC conversion interface of the PV generator.

### 5.1. Fault Modelling

Boost converters are acquiring more and more popularity in many electrical applications, particularly in renewable energy conversion systems [24,25]. In this application, the boost converter usually experiences excess electric and thermal stress [26], potentially leading to failure of the components. According to one survey, power semiconductor devices are considered the most fragile components [12]. The appearance of faults in one or more components can lead to degraded system performance, discontinuity of operations, and damage to the whole system. For this reason, it is crucial to promptly detect and isolate faults. Moreover, it is necessary to make early decisions around how to balance the continuity of system operations with the required performance and safety levels [27].

The boost converter is known for two fundamental faults, namely, open- and short-circuit faults [28]. The theme of diagnosing open-circuit faults in boost converters has garnered the attention of numerous researchers, with several diagnostic methods proposed in the literature [29].

In this paper, an additive actuator fault is investigated for the DC–DC boost converter depicted in Figure 6. The control signal is modeled as follows [28]:

$$u(k) = u_0 + f(k), \qquad (23)$$

where $u_0$ is the nominal control and $f(k)$ is the additive fault effect. For an open-circuit fault, the switches $S_{oc}$ are open. The dynamic response of the system is described as $u(k) = 0$, which can be satisfied under the following fault condition [13]:

$$f(k) = -u_0, \ \forall t \geq t_f. \qquad (24)$$

The primary contribution of this article involves the detection of open-circuit faults in a DC–DC converter within a networked photovoltaic system (see Figure 7). Any fault occurring in the DC–DC converter is bound to degrade the performance of the photovoltaic system, leading to alterations in current and voltage sensor readings. Consequently, adjustments to the control law become necessary. The exchange of packets among system sensors, the controller, and the DC–DC converter is intended to take place through network communication. However, any packet loss within this communication framework may heighten the control complexity, potentially compromising system performance and even precipitating system instability.
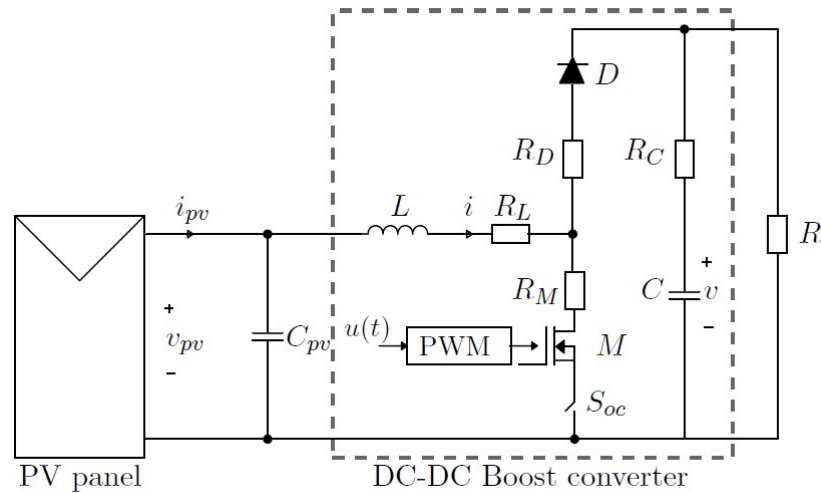
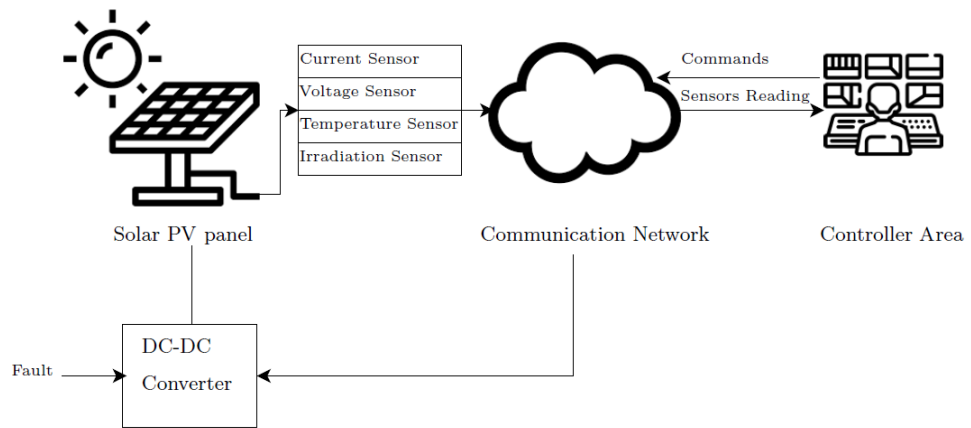**Figure 6.** Open-circuit fault model.



**Figure 7.** Defective DC–DC converter in a networked PV system.

*5.2. Observer-Based FDI System*

The main idea behind this approach is to generate a residual signal $r(k)$ that is sensitive to open- or short-circuit switch faults while being insensitive to variations in the PV current or voltage caused by changes in temperature and irradiation throughout the day. Here, $r(k)$ is generated through the residual generator system using the input and output information of the boost converter. In this way, the control law can be written as follows:

$$u(k) = \sum_{p=1}^{s} h_p(z(k)) K_p \hat{x}(k) \tag{25}$$

and the global system dynamics can be represented as

$$
\begin{aligned}
x(k+1) &= \sum_{p=1}^{s} h_p(z(k))(\bar{A}_p x(k) + \bar{B}_p \bar{u}(k) + \bar{B}_p f(k)), \\
&= \sum_{p=1}^{s} h_p(z(k))[(\bar{A}_p + \beta(k)\bar{B}_p K_p)x(k) - \beta(k)\bar{B}_p K_p e(k) + (1 - \beta(k))\bar{B}_p K_p x(k-1) \\
&\quad - (1 - \beta(k))\bar{B}_p K_p e(k-1) + \bar{B}_p f(k)].
\end{aligned}
\tag{26}
$$

The developed FD filter is represented

$$\hat{x}(k+1) = \sum_{p=1}^{s} h_p(z(k))(\bar{A}_p \hat{x}(k) + \bar{B}_p u(k) + L_p \bar{C}_p(\alpha(k)e(k) - (1 - \alpha(k))e(k-1)),$$

$$r(k) = \sum_{p=1}^{s} h_p(z(k))V\bar{C}_p(\alpha(k)e(k) - (1 - \alpha(k))e(k-1)). \tag{27}$$

The state estimation error is defined as

$$e(k+1) = x(k+1) - \hat{x}(k+1). \tag{28}$$

From Equations (26) and (28), the closed-loop system can be obtained as follows:

$$\phi(k+1) = \sum_{p=1}^{s} h_p(z(k))\hat{\mathscr{A}}_p \phi(k) + \hat{\mathscr{B}}_p \phi(k-1) + \mathscr{D}_p \vartheta(k) \tag{29}$$

where

$$\phi(k) = [x(k) \ e(k)]', \ \vartheta(k) = [f(k) \ 0]',$$

$$\hat{\mathscr{A}}_p = \begin{bmatrix} \bar{A}_p + \beta(k)\bar{B}_p K_p & -\beta(k)\bar{B}_p K_p \\ \beta(k)\bar{B}_p K_p - \bar{B}_p K_p & \bar{A}_p + \bar{B}_p K_p - \beta(k)\bar{B}_p K_p - \alpha(k)L_p \bar{C}_p \end{bmatrix},$$

$$\hat{\mathscr{B}}_p = \begin{bmatrix} (1 - \beta(k))\bar{B}_p K_p & -(1 - \beta(k))\bar{B}_p K_p \\ (1 - \beta(k))\bar{B}_p K_p & -(1 - \beta(k))\bar{B}_p K_p - (1 - \alpha(k))L_p \bar{C}_p \end{bmatrix}, \text{ and } \mathscr{D}_p = \begin{bmatrix} \bar{B}_p & 0 \\ \bar{B}_p & 0 \end{bmatrix}.$$

Assuming zero initial condition, we consider the following index:

$$J_k = \mathbb{E}\left\{ \sum_{k=0}^{N-1} [r'_k r_k - \delta^2 \vartheta'_k \vartheta_k] \right\} = \mathbb{E}\left\{ \sum_{k=0}^{N-1} [r'_k r_k - \delta^2 \vartheta'_k \vartheta_k + V_{k+1} - V_k] \right\} - V_N,$$

$$= \mathbb{E}\left\{ \sum_{k=0}^{N-1} [r'_k r_k - \delta^2 \vartheta'_k \vartheta_k + \Delta V_k] \right\} - V_N \leq \mathbb{E}\left\{ \sum_{k=0}^{N-1} [r'_k r_k - \delta^2 \vartheta'_k \vartheta_k + \Delta V_k] \right\} < 0. \tag{30}$$

The evaluation of the residual function and the threshold $J_{th}$ are defined as

$$J_k = \mathbb{E}\left\{ \sum_{\rho=k_0}^{k_0+k} \sqrt{r'(\rho)r(\rho)} \right\}, \tag{31}$$

$$J_{th} = \sup_{\vartheta_k \in L_2, f_k=0} \mathbb{E}\left\{ \sum_{\rho=k_0}^{k_0+k} \sqrt{r'(\rho)r(\rho)} \right\}, \tag{32}$$

where $k_0$ denotes the initial evaluation time instant.

As illustrated in the FDI diagram shown in Figure 8, the window size continuously increases until it equals the limited size of the global observation horizon, then $J_{th}$ is compared to $J_{th}$ to identify whether a fault has occurred:

$$\begin{aligned} J_k > J_{th} &\Rightarrow \text{Alarm for fault} \\ J_k \leq J_{th} &\Rightarrow \text{No fault.} \end{aligned} \tag{33}$$
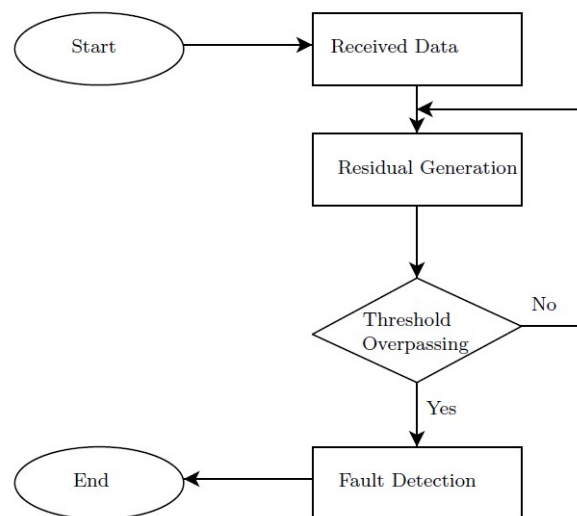
**Figure 8.** Diagram of the FDI algorithm.

To calculate the observer gain $L_p$, which enables the detection of faults as they occur, we apply the following Theorem.

**Theorem 2.** *Given a positive constant $\delta$, if there exist matrices $\mathscr{P}_i > 0$ and $\mathscr{Q} > 0$ satisfying the inequality*

$$\begin{bmatrix} -\hat{\mathscr{X}}_i & \hat{\mathscr{A}}_p & \hat{\mathscr{B}}_p & \mathscr{D}_p \\ * & -\mathscr{P}_i + \mathscr{Q} + (0_{1\times3}, 1) & 0 & 0 \\ * & * & -\mathscr{Q} & 0 \\ * & * & * & -\delta^2 \end{bmatrix} < 0, \quad i \in [1,4], \tag{34}$$

*then System* (29) *is asymptotically stable.*

**Proof.** To ensure the stochastic stability of System (29), we employ a similar proof technique to that in Theorem 1 while taking into account the updated values of the matrices.  □

## 6. Simulation Results and Discussions

To validate the theoretical analysis, a networked PV system was tested in the Matlab environment using the data shown in Table A1. The dynamics of the global system are represented in the form of fuzzy matrices. In this study, information transmission between different system components occurs via a communication network with a transfer rate of 0.9, implying that 10% of the packets are lost during transmission. A Markov chain is employed, considering four states (as each switch can be either opened or closed); refer to Table 1, where the probability matrix is as follows:

$$\Pi = \begin{bmatrix} 0.1 & 0 & 0 & 0.9 \\ 0.05 & 0 & 0.05 & 0.9 \\ 0 & 0.02 & 0.08 & 0.9 \\ 0.03 & 0.04 & 0.03 & 0.9 \end{bmatrix}. \tag{35}$$

### 6.1. Networked MPPT Control

To assess the performance of LMI as outlined in Theorem 1, a series of simulations were conducted. These simulations were executed in two distinct scenarios: the standard scenario and the real-time weather data scenario.

Standard Scenario

In this scenario, we simulated the PV generator under a constant standard atmosphere with the irradiation fixed at $\lambda = 1000$ W/m$^2$ and the temperature set at 25 °C. The values of the parameters $\gamma$ and $\delta$ and the gains $K_p$ and $L_p$ were determined after solving the LMIs (15), where $\gamma = 0.85$ and $\delta = 0.0063$. The controller and observer gains obtained in this way are as follows:

$$K_p = \begin{bmatrix} 0 & -0.0031 & 0.0120 & 0 \end{bmatrix}, \; L_p = \begin{bmatrix} 0.0043 \\ 0 \\ 0 \end{bmatrix}, \; p \in \begin{bmatrix} 1 & 16 \end{bmatrix}.$$

The optimum PV power response $P_{\max}$ is illustrated in Figure 9. As depicted in the figure, the controlled system reaches the maximum power point despite the packet loss. This observation underscores the system's robustness and adaptive capability, ensuring that optimal power generation is maintained despite potential disruptions.
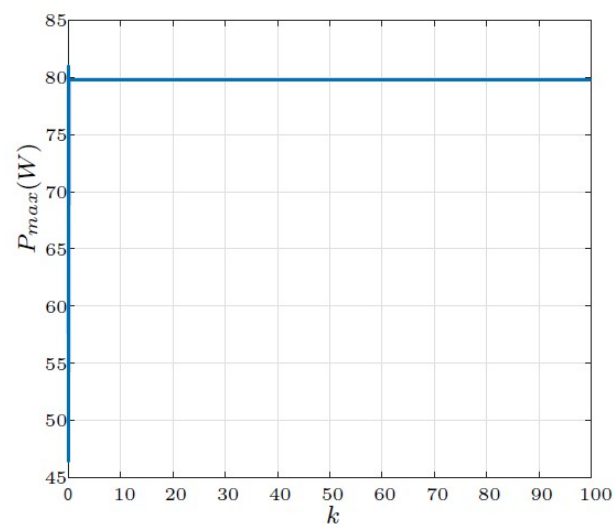


**Figure 9.** PV power response under standard conditions.

Real-Time Weather Data

In the second scenario, we explored the robustness of the proposed approach by incorporating empirical data. The aim of this study was to validate the effectiveness and reliability of our methodology through the utilization of real-world data in order to enhance the practical applicability of our approach. PV panel temperature and irradiation profiles were collected on 8 June 2020 from the weather station located at the Universidade Federal de Goiás (UFG) School of Electrical, Mechanical, and Computer Engineering (EMC), Goiânia, Brazil (data available freely at https://sites.google.com/site/sfvemcufg/weather-station). The data collected from the weather station are shown in Figure 10.

The PV power output response illustrated in Figure 11 demonstrates the adaptability of the control strategy, ensuring consistent attainment of the target power output. This adaptability remains robust even in the presence of daily fluctuations in weather conditions, including changes in temperature and irradiation. Moreover, the system demonstrates resilience against potential disruptions in data transmission between the sensor controller and the actuator, where in this case the actuator, refers to the DC–DC converter. Such robust performance underscores the effectiveness of the control strategy in sustaining the desired power output under various operational challenges.
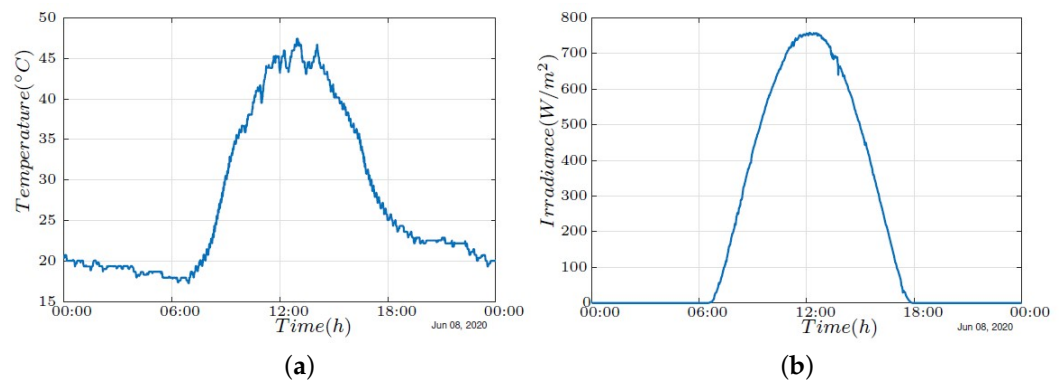
**Figure 10.** Two-day climatic data for (**a**) temperature and (**b**) irradiance.
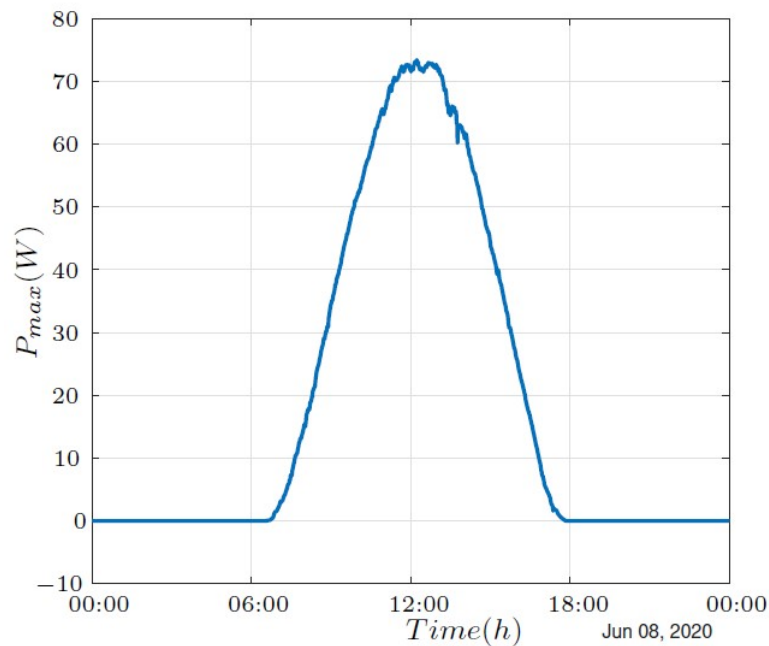


**Figure 11.** PV power response under real climatic conditions.

*6.2. Wireless Diagnosis*

This section presents the simulation results of the proposed wireless diagnosis strategy.

### 6.2.1. Normal Mode

In this section, a normal mode is studied in which no faults have been introduced. The solar panel parameters, including voltage and current, are illustrated in Figure 12. As shown in Figure 13, the PV power response aligns precisely with the characteristics outlined in the panel's specifications. Notably, our analysis reveals that the influence of packet loss is conspicuously absent from the plotted curve, affirming the robustness of the proposed approach. This underscores the capacity of our approach to mitigate the disruptive impact of network communication disturbances, thereby ensuring the constancy of key parameters. The presented figures vividly demonstrate the resilience of our approach, further validating its efficacy in maintaining stable system performance despite potential disruptions.
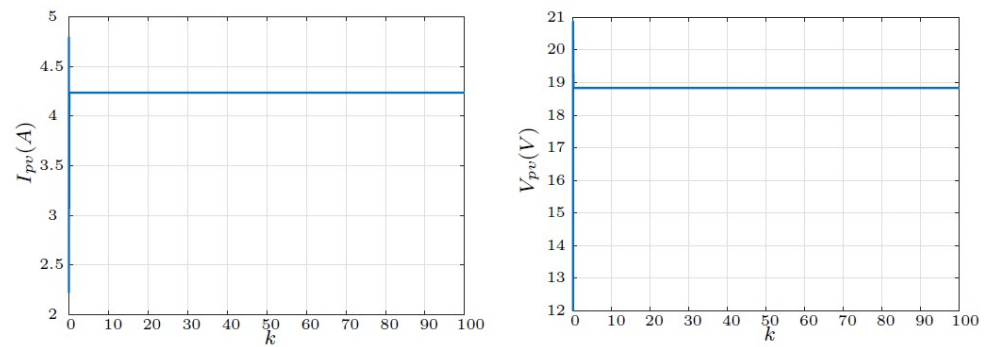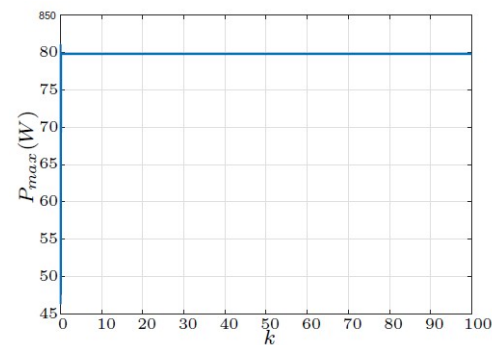
**Figure 12.** I–V characteristics of PV module.



**Figure 13.** PV power response.

Furthermore, our examination of the boost converter reveals a noteworthy outcome in that the output voltage $v$ surpasses that of the photovoltaic panel $v_{pv}$, as shown in Figure 14. This observation serves as compelling evidence substantiating the system's optimal performance even in the presence of communication challenges. Despite the existence of these disruptions, the boost converter consistently delivers an output voltage that exceeds the inherent panel voltage, affirming the robust and reliable nature of the proposed system.
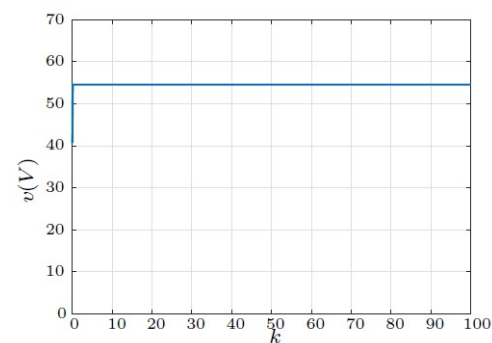


**Figure 14.** Output voltage $v$.

### 6.2.2. Faulty Mode

In this scenario, an evaluation of the proposed FDI strategy for DC–DC boost converters in PV systems was carried out considering an open-circuit switch fault at $k = 50$. As can be noticed from Figure 15, the panel voltage $v_{pv}$ increases to $21.5V$.
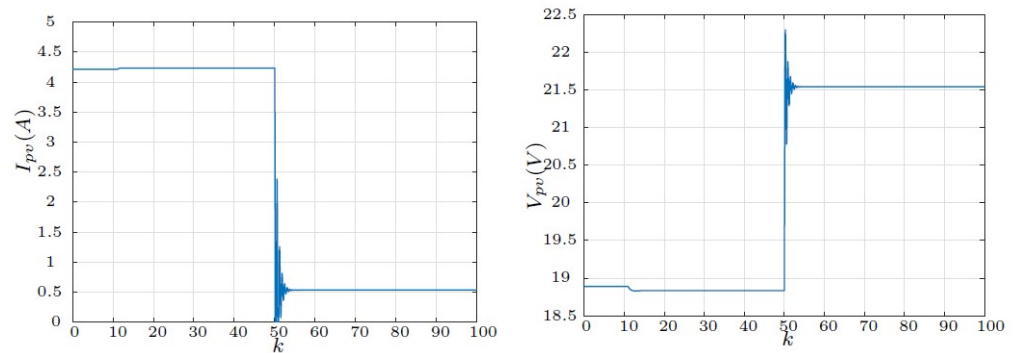
**Figure 15.** I–V characteristics of PV module.

On the other hand, the current drops to $0.5A$ after the appearance of the fault in Figure 15, representing a significant loss in power $P_{max}$, as shown in Figure 16. The output voltage of the boost converter decreases to a value significantly smaller than the panel voltage $v$ (refer to Figure 17), indicating the impact of the fault on the system.
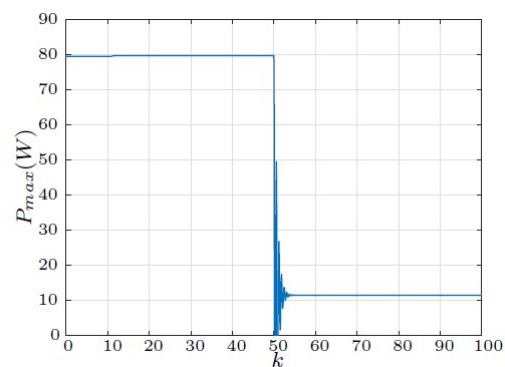


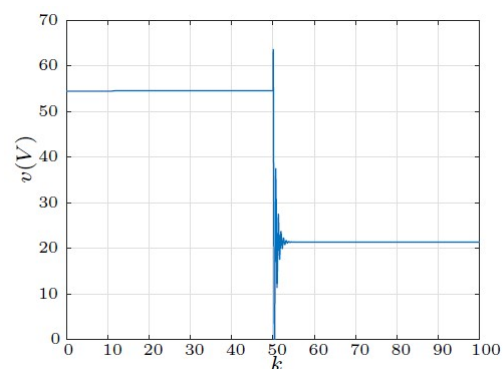**Figure 16.** PV power response.



**Figure 17.** Output voltage $v$.

Figure 18 plots the residual evaluation function $J_k$, which informs us of the time of occurrence and duration of the fault. The threshold is obtained, as $J_{th} = 56.9912$ for the size of the global observation horizon. It is noteworthy that FDI is achieved, indicating readiness to initiate the fault-tolerant control process. It is important to note that an open circuit switch fault is not a destructive fault, only resulting in poor efficiency under this fault condition. Despite the presence of packet dropout during the simulation, the residual evaluation function $J_k$ remains insensitive to variations in packet loss as well as in PV current and voltage while being sensitive to the open-circuit switch fault. This sensitivity reflects the effectiveness of the proposed filter.
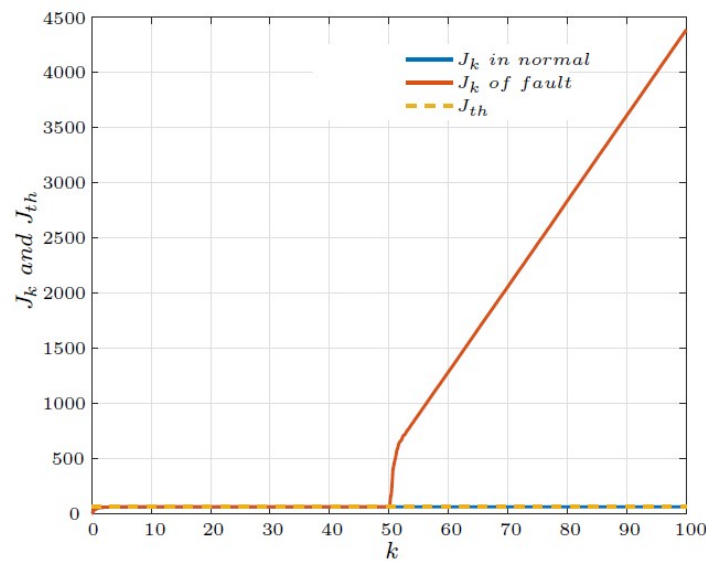
**Figure 18.** Evaluation of the residual function.

## 7. Conclusions

This paper introduces a cloud-based fault detection method for an MPPT boost converter in photovoltaic systems that is able to successfully detect open circuit switch faults. Leveraging the Lyapunov function and $H_\infty$ theory, the proposed approach formulates sufficient conditions as LMIs. Our simulation results validate the efficacy of the proposed method. Future research could extend this approach to account for the impact of packet dropout and communication delay on fault detection. Ultimately, this research advances the development of more reliable and efficient photovoltaic systems, offering a foundational framework for future studies to expand upon.

## Abbreviations

The following abbreviations are used in this manuscript:

| | |
|---|---|
| AC | Alternating Current |
| DC | Direct Current |
| FDI | Fault Detection and Isolation |
| LMIs | Linear Matrix Inequalities |
| MPPT | Maximum Power Point Tracking |
| MPPV | Maximum Power Point Voltage |
| NCS | Networked Control System |
| PV | Photovoltaic |
| PWM | Pulse Width Modulation |
| TS | Takagi–Sugeno |
| WSN | Wireless Sensor Network |

## Appendix A

**Table A1.** Simulation data.

| Parameters | Value | Unit |
|---|---|---|
| **PV Module** | | |
| Series-parallel cells $(N_s, N_p)$ | $(36, 1)$ | |
| Maximum power, $P_{max}$ | 80 | $W$ |
| Voltage at Maximum power, $V_{mp}$ | 18.2 | $V$ |
| Current at Maximum power, $I_{mp}$ | 4.4 | $A$ |
| Open circuit voltage, $V_{oc}$ | 21.5 | $V$ |
| Short circuit current, $I_{sc}$ | 4.91 | $A$ |
| **DC–DC Boost Converter** | | |
| Input capacitor, $C_{pv}$ | 1 | $mF$ |
| Output capacitor, $C$ | 100 | $\mu F$ |
| Output capacitor resistance, $R_C$ | 0.162 | $\Omega$ |
| Inductance, $L$ | 10 | $mH$ |
| Inductance resistance, $R_L$ | 0.48 | $m\Omega$ |
| Internal resistance of MOSFET, $R_M$ | 0.27 | $\Omega$ |
| Internal resistance of diode, $R_D$ | 0.24 | $\Omega$ |

## References

1. Zhang, T.; Yang, H. High efficiency plants and building integrated renewable energy systems: Building-integrated photovoltaics (BIPV). In *Handbook of Energy Efficiency in Buildings: A Life Cycle Approach*; Elsevier: Amsterdam, The Netherlands, 2018; pp. 441–595.
2. Simya, O.; Radhakrishnan, P.; Ashok, A.; Kavitha, K.; Althaf, R. Engineered nanomaterials for energy applications. In *Handbook of Nanomaterials for Industrial Applications*; Elsevier: Amsterdam, The Netherlands, 2018; pp. 751–767.
3. Kumar, N.M.; Chopra, S.S.; de Oliveira, A.K.V.; Ahmed, H.; Vaezi, S.; Madukanya, U.E.; Castañón, J.M. Solar PV module technologies. In *Photovoltaic Solar Energy Conversion*; Elsevier: Amsterdam, The Netherlands, 2020; pp. 51–78.
4. Akorede, M.F. Design and performance analysis of off-grid hybrid renewable energy systems. In *Hybrid Technologies for Power Generation*; Elsevier: Amsterdam, The Netherlands, 2022; pp. 35–68.
5. Hu, J.; Zhang, H.; Liu, H.; Yu, X. A survey on sliding mode control for networked control systems. *Int. J. Syst. Sci.* **2021**, *52*, 1129–1147. [CrossRef]
6. Duo, W.; Zhou, M.; Abusorrah, A. A survey of cyber attacks on cyber physical systems: Recent advances and challenges. *IEEE/CAA J. Autom. Sin.* **2022**, *9*, 784–800. [CrossRef]
7. Yaacoub, J.P.A.; Salman, O.; Noura, H.N.; Kaaniche, N.; Chehab, A.; Malli, M. Cyber-physical systems security: Limitations, issues and future trends. *Microprocess. Microsystems* **2020**, *77*, 103201. [CrossRef] [PubMed]
8. Hu, J.; Zhang, H.; Yu, X.; Liu, H.; Chen, D. Design of sliding-mode-based control for nonlinear systems with mixed-delays and packet losses under uncertain missing probability. *IEEE Trans. Syst. Man Cybern. Syst.* **2019**, *51*, 3217–3228. [CrossRef]
9. Xiaoli, X.; Daoe, Q. Remote monitoring and control of photovoltaic system using wireless sensor network. In Proceedings of the 2011 International Conference on Electric Information and Control Engineering, IEEE, Wuhan, China, 15–17 April 2011; pp. 633–638.
10. Hussain, S.S.; Khattak, K.S.; Khan, A.; Khan, Z.H. Cyber physical system for solar energy monitoring. In Proceedings of the 2019 International Conference on Frontiers of Information Technology (FIT), IEEE, Islamabad, Pakistan, 16–18 December 2019; pp. 185–1855.
11. Martin, A.D.; Cano, J.M.; Herrera, R.S.; Vazquez, J.R. Wireless sliding MPPT control of photovoltaic systems in distributed generation systems. *Energies* **2019**, *12*, 3226. [CrossRef]
12. Yang, S.; Bryant, A.; Mawby, P.; Xiang, D.; Ran, L.; Tavner, P. An industry-based survey of reliability in power electronic converters. *IEEE Trans. Ind. Appl.* **2011**, *47*, 1441–1451. [CrossRef]
13. Espinoza-Trejo, D.R.; Diez, E.; Barcenas, E.; Verde, C.; Espinosa-Perez, G.; Bossio, G. Model-based fault detection and isolation in a MPPT boost converter for photovoltaic systems. In Proceedings of the IECON 2016-42nd Annual Conference of the IEEE Industrial Electronics Society. IEEE, Florence, Italy, 23–26 October 2016; pp. 2189–2194.
14. Benzaouia, A.; Telbissi, K. Actuator fault estimation based on proportional integral observer for discrete-time switched systems. *J. Dyn. Syst. Meas. Control.* **2019**, *141*, 31011. [CrossRef]
15. Cano, J.M.; Martin, A.D.; Herrera, R.S.; Vazquez, J.R.; Ruiz-Rodriguez, F.J. Grid-connected PV systems controlled by sliding via wireless communication. *Energies* **2021**, *14*, 1931. [CrossRef]
16. Rivai, A.; Abd Rahim, N.; Mohamad Elias, M.F.; Jamaludin, J. Analysis of photovoltaic string failure and health monitoring with module fault identification. *Energies* **2019**, *13*, 100. [CrossRef]
17. Shariff, F.; Abd Rahim, N.; Hew, W.P. Zigbee-based data acquisition system for online monitoring of grid-connected photovoltaic system. *Expert Syst. Appl.* **2015**, *42*, 1730–1742. [CrossRef]
18. Aatabe, M.; El Guezar, F.; Bouzahir, H.; Vargas, A.N. Constrained stochastic control of positive Takagi-Sugeno fuzzy systems with Markov jumps and its application to a DC-DC boost converter. *Trans. Inst. Meas. Control.* **2020**, *42*, 3234–3242. [CrossRef]

19. Khabou, H.; Souissi, M.; Aitouche, A. MPPT implementation on boost converter by using T–S fuzzy method. *Math. Comput. Simul.* **2020**, *167*, 119–134. [CrossRef]

20. Aatabe, M.; El Guezar, F.; Vargas, A.N.; Bouzahir, H. A novel stochastic maximum power point tracking control for off-grid standalone photovoltaic systems with unpredictable load demand. *Energy* **2021**, *235*, 121272. [CrossRef]

21. Tanaka, K.; Wang, H. *Fuzzy Control Systems Design and Analysis: A Linear Matrix Inequality Approach*; John Wiley & Sons: New York, NY, USA, 2002.

22. Wang, Z.; Ho, D.W.; Liu, X. Variance-constrained filtering for uncertain stochastic systems with missing measurements. *IEEE Trans. Autom. Control.* **2003**, *48*, 1254–1258. [CrossRef]

23. Fard, M.; Aldeen, M. Robust control design for a boost converter in a photovoltaic system. In Proceedings of the 2016 IEEE 7th International Symposium on Power Electronics for Distributed Generation Systems (PEDG), IEEE, Vancouver, BC, Canada, 27–30 June, 2016; pp. 1–9.

24. Soon, J.L.; Lu, D.D.C. A simple open-circuit fault detection method for a fault-tolerant DC/DC converter. In Proceedings of the 2015 IEEE 11th International Conference on Power Electronics and Drive Systems, IEEE, Sydney, Australia, 9–12 June 2015; pp. 98–103.

25. Shahbazi, M.; Jamshidpour, E.; Poure, P.; Saadate, S.; Zolghadri, M.R. Open-and short-circuit switch fault diagnosis for nonisolated DC–DC converters using field programmable gate array. *IEEE Trans. Ind. Electron.* **2012**, *60*, 4136–4146. [CrossRef]

26. Lu, B.; Sharma, S.K. A literature review of IGBT fault diagnostic and protection methods for power inverters. *IEEE Trans. Ind. Appl.* **2009**, *45*, 1770–1777.

27. Jagtap, S.; More, D. Switch Open-circuit Fault Diagnosis and Fault-Tolerant Control for Boost DC-DC Converter. *Procedia Comput. Sci.* **2020**, *171*, 934–940. [CrossRef]

28. Espinoza Trejo, D.R.; Bárcenas, E.; Hernández Díez, J.E.; Bossio, G.; Espinosa Pérez, G. Open-and short-circuit fault identification for a boost dc/dc converter in PV MPPT systems. *Energies* **2018**, *11*, 616. [CrossRef]

29. Bento, F.; Cardoso, A.J.M. Open-circuit fault diagnosis and fault tolerant operation of interleaved DC–DC boost converters for homes and offices. *IEEE Trans. Ind. Appl.* **2019**, *55*, 4855–4864. [CrossRef]